VISUALIZING THE FLOW INDUCED BY AN AIR CURTAIN OVER A MANNEQUIN USING STEREO PARTICLE IMAGE VELOCIMETRY

by

JOHN EDWARD FERNANDES

Presented to the Faculty of the Graduate School of

The University of Texas at Arlington in Partial Fulfillment

of the Requirements for the Degree of

MASTER OF SCIENCE IN MECHANICAL ENGINEERING

THE UNIVERSITY OF TEXAS AT ARLINGTON

December 2008

ACKNOWLEDGEMENTS

I wish to thank my advisor, Dr. Frank Lu of the Department of Mechanical and Aerospace Engineering. Dr. Lu has been ever supportive and patient with his guidance throughout the course of my thesis work. I would specially like to thank him for his constant support in helping me secure financial aid throughout the course of my studies.

I wish to thank the other members of my defense committee, Dr. Robert Woods and Dr. Donald Wilson, for presiding over my thesis defense and providing the necessary acknowledgement of the same.

I specially wish to thank Adam Pierce for teaching me all that was needed to know about the working of the stereo particle image velocimetry system. Without his guidance, I would be far from done with my experimental work.

I also wish to thank Eric Braun, Richard Mitchell and my other colleagues at the Aerodynamics Research Center for their guidance and advice.

Finally, I wish to thank my father and brother for their constant support, advice, prayers and words of encouragement. I would dearly wish to thank my mother, who is not with us anymore, for her guidance, love and prayers.

July 17, 2008

ABSTRACT

VISUALIZING THE FLOW INDUCED BY AN AIR CURTAIN OVER A MANNEQUIN USING STEREO PARTICLE IMAGE VELOCIMETRY

John Edward Fernandes, M.S.

The University of Texas at Arlington, 2008

Supervising Professor: Frank K. Lu

Air curtains find widespread applications in today's world, such as in malls, supermarkets, airports, cold storage, etc., to allow easy pedestrian movement between two different environments. There is interest in understanding the flow induced by traffic through the air curtain in terms of energy efficiency and the ability to provide isolation from contaminants and airborne pathogens. To develop an understanding of the flow, an initial exploratory study was performed using a static mannequin.

A stereo particle image velocimetry (SPIV) system was set up to map the flow of the air curtain, installed on top of the doorway, over a mannequin. The mannequin, dressed in a black, long sleeved shirt and matching track pants, was placed in the center of the doorway and directly under the air curtain. Two sets of maps were obtained, one parallel to the plane of the jet and the other perpendicular to it. In the first case, three parallel, vertical planes were mapped, starting within the plane of the jet and the others away from it and towards the cameras. In the second case, one vertical plane, which was incident to and at the center of the doorway, without the mannequin was mapped. In either case, each plane was divided into

smaller regions which were recorded one at a time. Stereo pairs of 400 images were obtained for each region and then ensemble averaged. The arrays were then stitched together to provide the final, seamless dataset.

The velocity maps indicated a low velocity region around the mannequin as compared to the adjoining areas as well as a clear obstruction to the output flow from the air curtain. A high turbulence region was located close to where the air curtain jet and the mannequin first meet. The incident plane, which was recorded to give a general prediction of the flow from the air curtain, indicated a certain unsteadiness of the output flow. This, however, was caused by a clear lack of recorded data. Overall, the results indicate the successful implementation of the PIV system in visualizing the flow from an air curtain over a mannequin.

TABLE OF CONTENTS

LIST OF ILLUSTRATIONS

LIST OF TABLES

CHAPTER 1

INTRODUCTION

1.1 Previous Studies of Air Curtains

An air curtain or air door is a device used to separate two different spaces or environments while permitting easy and steady pedestrian and material movement between the two. A very common application is at the entrance to a building, where it helps to keep the outside air out and avoid cold draught by mixing warm air from the air curtain. In addition to this, an air curtain also provides an energy efficient, thermal barrier [1-3]. Therefore, air curtains are frequently used in conjunction with refrigerated rooms and cold storage [4-5]. Being a transparent barrier, it provides an unobstructed view of the interior, which makes air curtains ideal for refrigerated displays [6-7]. In addition to those stated above, air curtains find other widespread application in today's world [8] and are the subject of much commercial development. The versatility of air curtains permits them to find application in indoor climate control; pest control [9]; industrial ovens and smoke, dust or fume control [10-13].

The scientific study of air curtains can be traced to the 1950s and 60s [14-16]. The studies found that an important consideration in designing air curtains is the ability to maintain a narrow planar jet so as to provide a thin dynamic barrier with minimum entrainment [17-18]. In addition, studies reported that there were numerous parameters that affect the performance of air curtains. However, the experimental study of air curtain flows was hampered by facility and instrumental limitations. For example, using laborious point measurements [19] made the acquisition of large datasets difficult, if not impossible. With the recent advances in instrumentation and data processing techniques, former experimental methods have been replaced by flow visualization [20]. Particle image velocimetry [17,21-22], thermography [23-24]

and computer modeling [22,25-26] are examples of the same. The present study employs the principle of stereo particle image velocimetry for large-field mapping of air curtain flow.

There is precedence in using mannequins for studying ventilation and natural convection associated with human activities. Both heated and unheated mannequins [27-29] have been employed with the former simulating the actual thermal state of humans [30-34]. Unheated mannequins are used where a forced convective flow exists. A recent study of the human thermal plume showed that the maximum plume velocity is 0.24 m/s [35]. Comparing this against the maximum velocity of the flow leaving the air curtain of the present study of 5.8 m/s [36], one can conclude that the human plume is negligible. Thus, the isothermal mannequin is deemed adequate for the present study. An alternate justification of an isothermal mannequin can be based on buoyancy considerations. Buoyancy effects are negligible for low values of the Richardson number $Ri = \left(\rho_{amb} - \rho_{jet}\right)gh / \rho_{amb} V_{jet}^2$. In a study of cold wall jets pertaining to air curtains [26], the justification for an isothermal assumption was that the low value of the Richardson number of 0.3. For the present case, a clothed human will have an average surface temperature of 26.6℃ [35]. With an ambient tempera ture of 20℃, a characteristic height of 2 m and a jet velocity of about 6 m/s, the Richardson number for the present experiment is about 0.01, that is, practically zero, thus amply justifying the use of an isothermal mannequin.

1.2 Particle Image Velocimetry

Particle image velocimetry, or PIV for short, is a non-intrusive, optical method used to measure velocity and related properties in fluids. It is a well-accepted approach for mapping velocity fields from micron to meter scales [37]. The principle revolves around the analysis of captured images of seeded flow, illuminated by a dual-pulse laser, by CCD cameras. A basic PIV setup has been illustrated in Fig. 1.1.

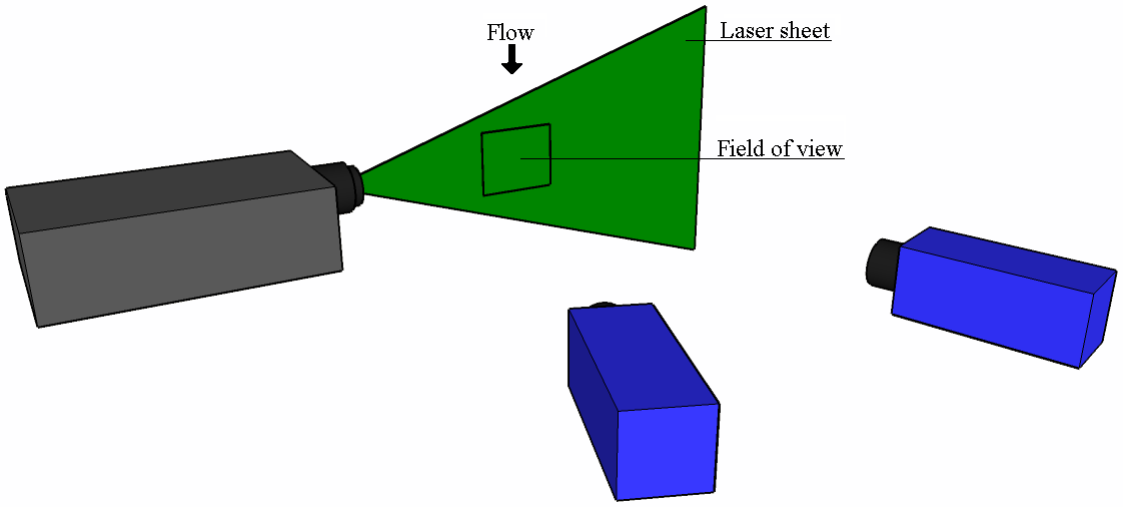

Figure 1.1 Basic experimental setup for PIV

The laser sheet is aligned with the plane, within the flow, to be surveyed. The cameras are oriented such that they focus on a common field of view within the plane. Depending upon the number of cameras employed, it is possible to map either a 2D or 3D flow field. With a single CCD camera, it is only possible to map the in-plane velocity. However, when employing two or more cameras it becomes possible to map in-plane, three-dimensional flow fields. In the current case, two ICCD cameras in a stereo arrangement were employed for the PIV surveys as depicted in Fig. 1.1.

The process of image capturing involves the synchronization of both the laser and the cameras such that the cameras only capture images when the laser pulses. In this way, distinct images of the flow can be obtained in the dark which gives reliable intensity information for processing and velocity vector calculation. Two images, one at each laser pulse, are captured by each camera at any time or position. These two images collectively contain the flow information for the time Δt, which is the period between the two laser pulses. Depending upon the resolution of the cameras, each image is divided into many square interrogation regions, each of which gives a velocity vector. Cross-correlation of intensity values is employed over the area of the interrogation windows, located at the same position on each of the two images. The

position of the correlation peak from the center of the plot gives us the magnitude and direction of the mean displacement of the particles in the selected region. By dividing the magnitude of the displacement by the time period Δt, we get the mean velocity of the particles or the flow in general. This procedure is shown schematically in Fig. 1.2.

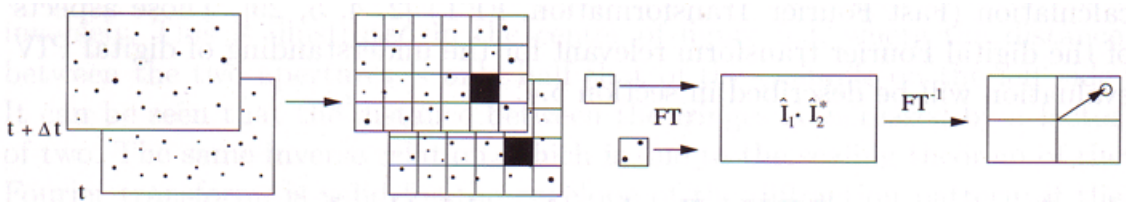

Figure 1.2 Calculation of velocity vectors using cross-correlation by FFT of the intensity values from the captured images [38]

In stereo particle image velocimetry (SPIV), a velocity vector field is obtained for each camera. However, since the view from each camera is inclined, mathematical equations are employed to combine the two fields to get a single corrected image [39]. Using the velocity values thus obtained, derived properties such as turbulence kinetic energy and Reynolds stress as well as streamlines, streaklines and pathlines can also be obtained.

1.3 Objectives of Present Study

The focus of the experiments was to the study the influence of the mannequin present in the air curtain using stereo particle image velocimetry. This involves mapping a large area in order to obtain statistical properties of the jet plume.

Chapter 2 highlights the two experimental setups which were employed to map planes which were perpendicular to each other. The chapter also provides a detailed description of the apparatus used in the experiments and the settings under which they were employed. The procedure for recording images as well as the processing of the same are also explained. In chapter 3, detailed maps of the mean velocity, the turbulence kinetic energy and the Reynolds stresses that were obtained for both the parallel as well as perpendicular planes are analyzed to improve the understanding of air curtain flows.

Chapter 4 highlights the overall conclusions drawn from the study and the results thereof. Recommendations for improving the analysis as well as future work for enabling the same have been highlighted as well.

CHAPTER 2

EXPERIMENTAL METHODS

A test cabin was built to ensure a well-defined flow from the air curtain. The general layout of the test cabin is a 2.4 m cube consisting of a floor, walls, a ceiling and the doorway. The cabin was partitioned midway by a 0.15 m thick wall with a 0.91 m wide and 2.1 m tall doorway. A Fantech Model AC3600 air curtain was mounted at the top of the doorway. Figure 2.1 shows a cutaway view of the test cabin, less the ceiling, and the front and left walls.

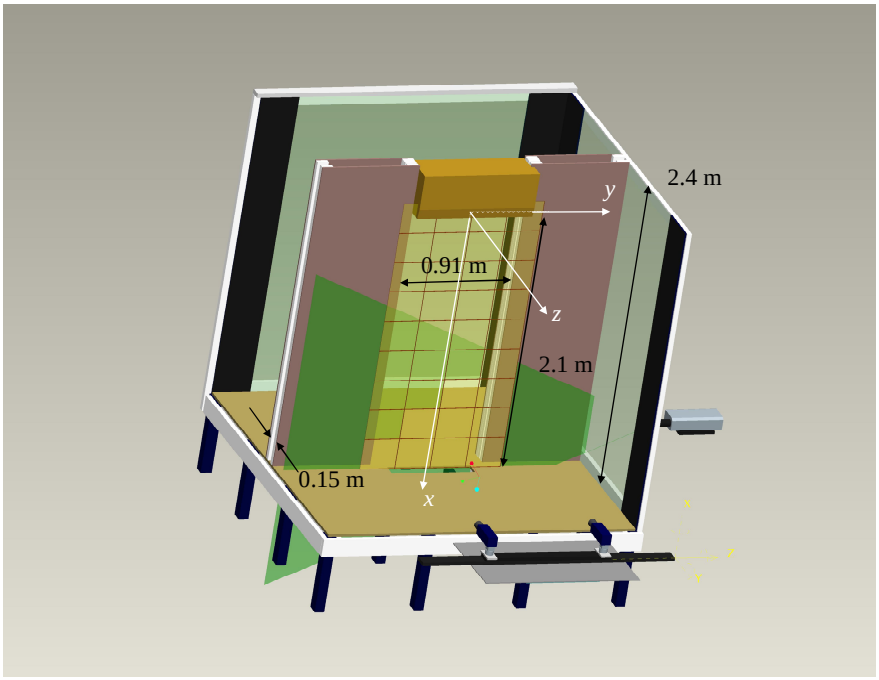

Figure 2.1 Cutaway view of the test cabin

The facility was raised 0.6 m from the laboratory floor to accommodate ducting. The air curtain is capable of delivering a maximum flow velocity of 10.3 m/s and a maximum flow rate of 22.5 m^3/min. The housing on the air curtain was locked to ensure flow in only the downward direction. The exhaust of the air curtain was directed through a grilled vent comprising of a grid

of six rows of 25 rectangular openings, each 30 mm long and 10 mm wide, with a total area of 0.0444 m^2. The flow was produced by a fan in the air curtain and captured by two floor vents directly below the air curtain. The vents were covered by two registers (Home Depot Model No. 4151004BR), each 101.6 mm wide and 304.6 mm long. The total open area of the floor vents was approximately equal to the open area of the air curtain exhaust vent. Upon passing the floor vent, the air entered a 0.0084 m^3 plenum. The air then traveled through a 305 mm diameter air conditioning duct which redirected it to the roof of the cabin, entering the diffuser, which was located approximately 1.07 m behind the air curtain unit. The diffuser, shown in Fig. 2.2, was installed to smoothen out the flow of air through it and direct it to the front portion of the air curtain. Figure 2.3 shows the air curtain mounted just ahead of the doorway with the mannequin positioned below it.

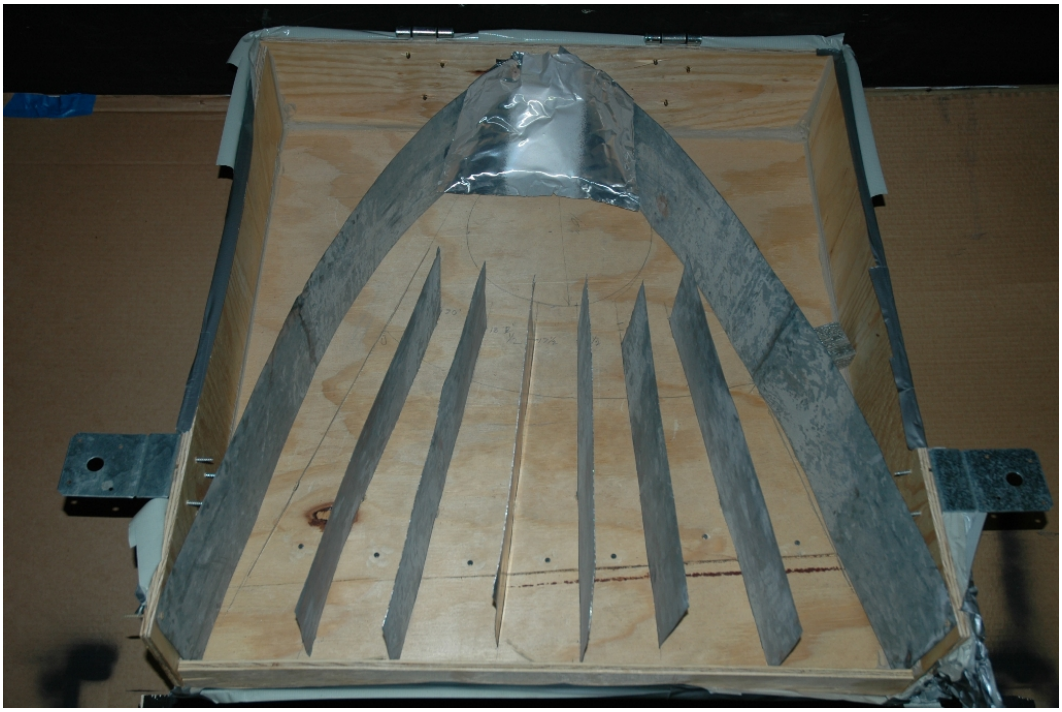

Figure 2.2 Photograph of guide vanes of the wide-angle diffuser supplying air to the air curtain

A commercial, white male mannequin, standing 1.84 m tall (Rudy1/F, Mondo Mannequins, New York), was placed in the doorway as shown in Fig. 2.3. The widest dimension

of the mannequin is 546 mm measured from the knuckles of both hands. The mannequin was dressed in a black cotton tracksuit with the head, hands and feet exposed. The black color was chosen so as to minimize the reflections caused by the incident laser beam. The original tempered glass stand of the mannequin was replaced by a smaller acrylic stand as the former blocked the floor vents when the mannequin was positioned under the air curtain. The center of the mannequin was 77.8 mm ahead of the leading edge, 443.9 mm from the left post and 466.1 mm from the right post of the doorway. The slight asymmetry was due to the slight offset of the air curtain to accommodate its switch at the right side of the doorway.

Figure 2.3 Photograph of air curtain mounted just ahead of the doorway with the mannequin

2.1 Hardware Components

The LaVision FlowMaster 3D system was employed for the stereo particle image velocimetry surveys. This system consists of the following components listed below.

2.1.1 Laser

A New Wave Research 120 Nd:YAG double-pulsed laser was employed for the surveys. It is capable of up to a 15 Hz pulse rate and 2 X 120 mJ/pulse at a wavelength of 532 nm. The entire laser setup was mounted on a portable stand to enable easy movement. The laser head was mounted on a pivot and guide to enable easy movement of the laser sheet in the vertical plane so as to guarantee complete and uniform illumination of the region to be recorded. The laser beam was spread into a 2.5 mm thick sheet by a cylindrical lens with a focal length of $f = -10$ mm, which allowed a working distance of 2000 mm. This fulfilled the distance requirement needed for the laser to properly illuminate the measurement area. A safety concern was the movement of the laser beam during alignment and calibration arising from stray reflections. This was problematic during the alignment of the laser and calibration plate. To overcome this problem, a Sears Craftsman 180° precision laser level, with its lower laser power, was used to sight the Nd:YAG laser. These two lasers are shown in Fig. 2.4.

Figure 2.4 The precision laser level mounted ahead of the Nd:YAG laser

2.1.2 Cameras and Lifting Mechanism

Two FlowMaster 3S ImagerIntense/ImagePro ICCD cameras were employed for image capturing. The cameras boast a 1376 X 1040 pixel resolution, a maximum framing rate of 10 Hz and a 12-bit dynamic range. At the base of the cameras were three knobs which permitted the rotation of the cameras about the x, y and z axes. The cameras were mounted on an indexed guideway and separated by 815 mm. This entire setup was mounted on a warehouse life (Genie Superlift™ Advantage Model SLA-15, Redmond, Washington, USA) as shown in Fig. 2.5, so as to achieve a vertical coverage of the survey by lifting the entire system up and down. This lift is capable of loads up to 383 kg and it can reach up to 5 m (16.3 ft). The front castors were removed to compensate for a vertical tilt in the lift system. The lift was operated by a manual low-speed winch at a rate of 0.38 cranks/cm for the low-speed setting. The high-speed setting was not employed.

Figure 2.5 Photograph showing the lifting mechanism with the stereo cameras

2.1.3 Seeder

Seeding for the particle image velocimetry system was provided by a LaVision V-Z Droplet Seeder shown in Fig. 2.6. Seed material was ordinary extra virgin olive oil. The outlet of the seeder was connected to the front portion of the cabin, at the floor, near the doorway by a plastic pipe. The seeder was run by compressed air from a rotary compressor delivering an average pressure of around 200 kPa. The seed particles were estimated to have a mean diameter of 1 μm. To seed the large volume of the test cabin, the seeder was first run for about 15 s with the air curtain on. This provided enough seed without saturating the cameras. The seeder was then disconnected from the compressor and a further minute was given to allow the uniform distribution of seed before recording. The seed concentration eventually decreased as the oil droplets started getting absorbed by the wooden structure and escaped through tiny leaks from the cabin into the room.

Figure 2.6 Seeder positioned under the cabin

2.1.4 Computer Setup

The other major components of the imaging system include a frame grabber, timing control electronics and a host computer, shown in Fig 2.7 (a) and (b), with dual Intel Xeon processors running the DaVis 7.1 data acquisition and processing software. Recorded data were stored in a 750 GB hard drive. Calibration, recording and processing of data for the surveys were carried out using DaVis. Also, the cameras and laser were synchronized at 5 Hz framing rates for the experiments.

(a) (b)

Figure 2.7 (a) Workstation provided by LaVision preloaded with DaVis 7.1, (b) Rear end of cabinet with cables from the laser and cameras

2.2 Experimental Setup

Since two \ perpendicular plane settings were mapped, the experimental setup was arranged to facilitate the successful recording of the same. In either case, the position of the laser was the only parameter which changed. This is because the laser has to be coplanar with the complete area that has to be surveyed.

2.2.1. Parallel Planes

The floor of the cabin had six parallel lines marked down, each at a specific distance from the front window, to indicate the positions at which the planes were to be recorded. Starting from the one nearest to the front, the lines were numbered six to one, while moving towards the doorway. The line numbered 1 was 1846.5 mm from the cameras' focal plane and was located at the center of the air curtain. The distances of demarcations two to six were 95.5, 76, 75, 154 and 151 mm from the previous line toward the cameras, respectively. Based on previous bare air curtain results, only positions one, three and four were selected for recording.

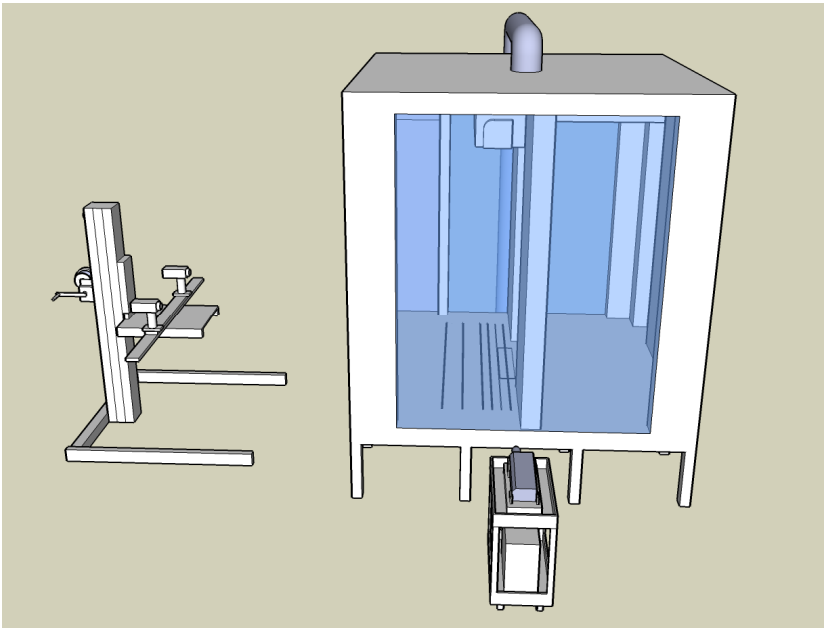

Figure 2.8 Experimental setup for recording the parallel planes

The laser, mounted on the portable trolley, was positioned at the side of the test cabin, as indicated in Fig. 2.8, such that the laser sheet was parallel to the demarcations at the bottom of the test cabin and shining from right to left while viewing from the front of the setup. The lift, with the cameras and railing mounted on it, was placed in front of the cabin with the cameras focusing on the doorway.

2.2.2 Perpendicular plane

The mannequin first was taken out so as to permit the surveying of the bare air curtain. The laser, which was previously placed to the side of the cabin, was mounted in between the cameras. Since the laser emits a sheet in only the upward direction, an elevated and inclined wooden base was fabricated, which fitted perfectly on the guiderails. The laser was then fastened to the base and the entire assembly was precisely positioned such that the laser sheet was equidistant from the two cameras. A new line was drawn on the floor of the test cabin to indicate the center of the doorway. The entire camera and laser assembly was then positioned such that the laser sheet and the new demarcation were coplanar. This position on the guiderails was then locked and the test setup was complete and ready for calibration and recording.

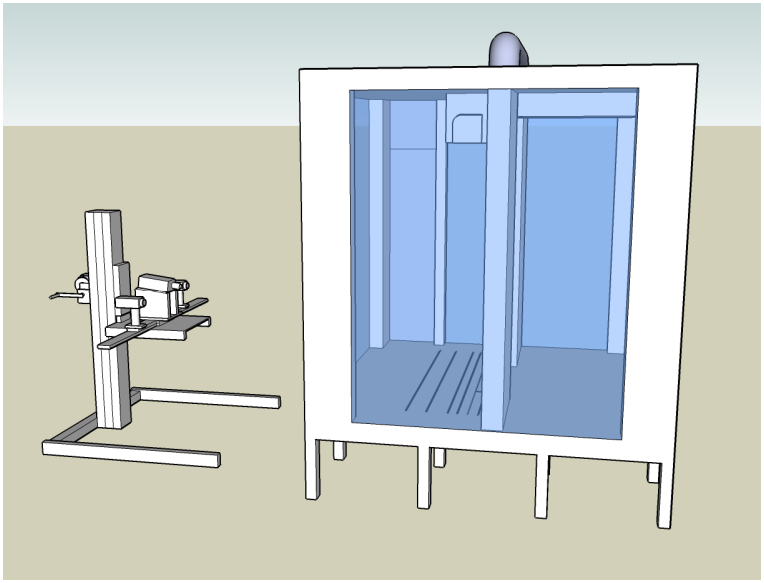

Figure 2.9 Experimental setup for recording the perpendicular plane

2.3 Recording and Processing

Before carrying out the preliminary steps of recording, it has to be ensured that all components of the experimental setup are ready for use. First, the computer and the cameras were switched on. The cameras took a while to reach their operational condition, with an indicator LED flashing red before glowing green to indicate that the cameras were ready for use. Once the computer and the cameras were ready for use, the DaVis software, preloaded on the computer, was executed. The cameras were detected during startup and the expert setting was chosen before the software displayed the main menu window. Next, the laser was turned on and set to standby allowing it to warm up for a while. The setup is was then ready for calibration.

2.3.1 Calibration of cameras

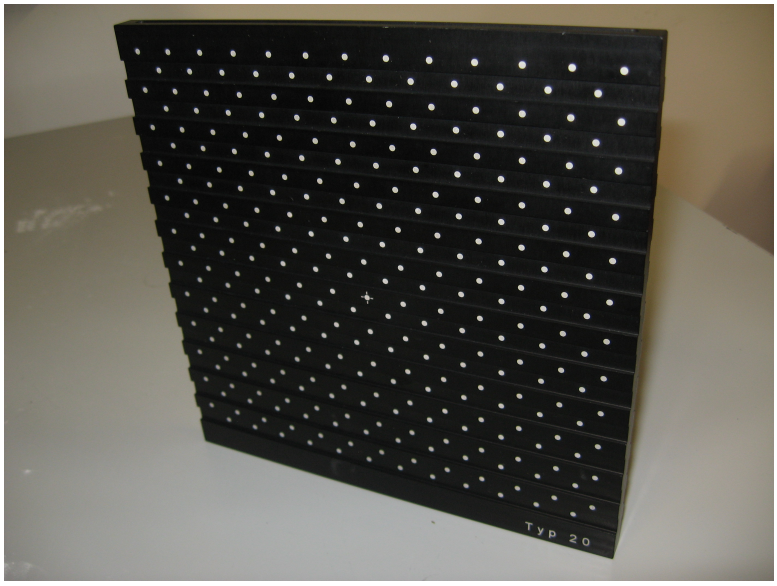

Figure 2.10 Calibration plate employed in the experiments

In order to ensure successful recording and processing, the cameras had to focus sharply on the region of interest. Also, the software should be able to take the pictures and apply accurate dimensional and intensity scales to them. This was facilitated by calibrating the cameras. A calibration plate was provided for this purpose, as seen in Fig. 2.10. The calibration plate, named Type #20, has a series of well defined and equally spaced white dots printed on

the flat surfaces of alternate crests and troughs on both large faces. Apart from the white dots, the calibration plate is jet black in color. The diameter of each dot is 2 mm and the distance between dots is 15 mm. The dot at the center of each face has a crosshair printed as well. The plate has a constant thickness of 12 mm. The plane to plane distance between any crest and trough is 1.5 mm. All specifications pertaining to the plate are preloaded in DaVis which can be recalled in the calibration wizard by choosing '#20' under the menu for the type of calibration plate. The plate is always oriented such that the face with the crosshair on a crest is facing the cameras.

Figure 2.11 Calibration plate and stand positioned in the test cabin

The calibration plate was attached to a stand which was placed in the test cabin. Both the plate and stand were positioned such that the plate was coplanar with the region that was to be surveyed. So, if parallel plane #1 was to be recorded, then the plate had to be aligned with the demarcation indicating the same at the floor of the cabin. Using a spirit level, the top surface of the plate was made perfectly horizontal to the floor of the test cabin. Once the plate and stand were setup for calibration, the next step was the positioning of the cameras. The lift was either raised or lowered such that the plate appeared at the center of each cameras image. This was accomplished by choosing the interactive mode in DaVis and setting the cameras to constantly grab images. The focus of each camera was adjusted such that a clear and sharp image of the calibration plate was obtained. The three adjustable knobs at the base of each camera were used to adjust the positions of the cameras are adjusted such that the central

crosshair of the calibration plate appeared at the geometric center of each image. Once this was achieved, the grabbing was stopped and the calibration wizard was initiated. In the wizard, there were eight steps that had to be successfully completed before the calibration was completed. The first three steps involved choosing the type of camera setup, the coordinate system and the type of calibration plate. The cameras were setup as a pair, mapping in stereo configuration. The coordinate system was right-handed and the type of calibration plate used was 'Type #20'. The next step, called image acquisition, involved capturing a clear image from each camera. As the cameras were already positioned and focused prior to entering the calibration wizard, the only operation carried out in this step was capturing an image from each camera. The next four steps describes the actual calibration of the cameras.

The fifth step required the user to define three specific points on the calibration plate in each of the two images so that the wizard can search and mark the remaining points. For the sake of reducing error, the middle crosshair, the dot on the following crest directly below it and the dot to the immediate right of the latter were chosen. Since the points were chosen at the center, error in locating the dots towards the edges of the calibration plate was reduced. Positioning the marks at the center of each of three dots is vital to reducing the rms error in calibration. Therefore, the zoom function was employed and the marks were precisely positioned at the center of each dot. In the sixth step, the wizard utilized the previous mark definition, the clear contrast between the dots and the black background in each image and the inherent plate information to mark all the remaining dots on the front surface of the calibration plate. If the previous mark definition was not carried accurately, the wizard may fail to recognize and select each and every point on the calibration plate. To obtain a good calibration, it was essential that the wizard was able to search and select each and every dot on the plate. Therefore, most time spent in calibration was spent in alternating between steps five and six till the user had obtained satisfactory results. In the last two steps of calibration, the calculation of the fit mapping function and the evaluation of corrected images were carried out. In calculating

the fit mapping function, an rms fit error was obtained and it was vital that this value be kept below 10. Normally, an rms fit error of around 0.11 for both cameras is considered to be a very good result. In the final step, the wizard combines the two images to get a single corrected image displaying a grid with a dot at the intersection of every grid line. All values pertaining to the cameras, such as the image dewarping function, the focal length, the distance of both cameras along the z axis from the calibration plate, etc. were calculated. Once step eight was completed, the calibration settings were saved, the plate and stand were removed from the cabin and the experimental setup was ready for recording.

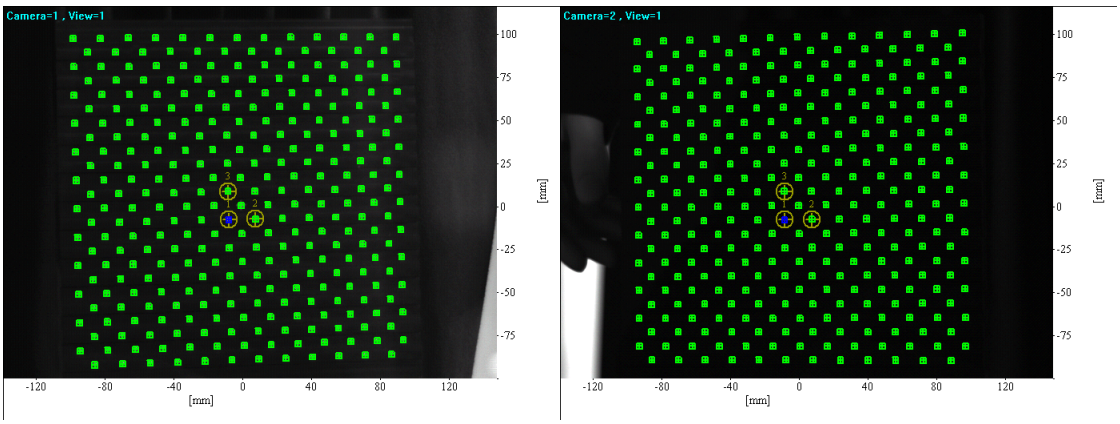

(a) (b)

Figure 2.12 Mark definition and searching for (a) Camera 1 and (b) Camera 2

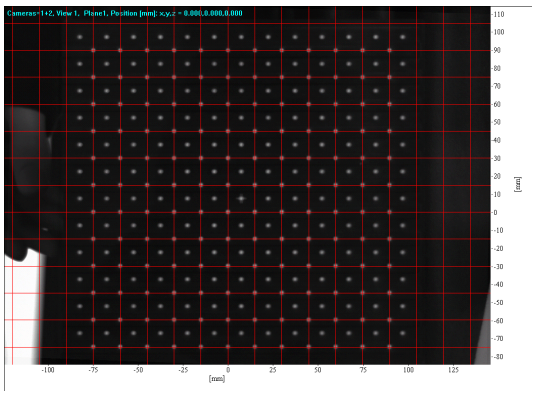

Figure 2.13 Corrected image generated at the end of calibration for a parallel plane setting

Calibration for the perpendicular plane is the same as above, except that the calibration plate was oriented perpendicular to the air curtain jet and positioned at the center of it. Also, each camera focused on a different side of the calibration plate and the mark definition was carried out such that all three points were located at exactly the same position on either side of the plate.

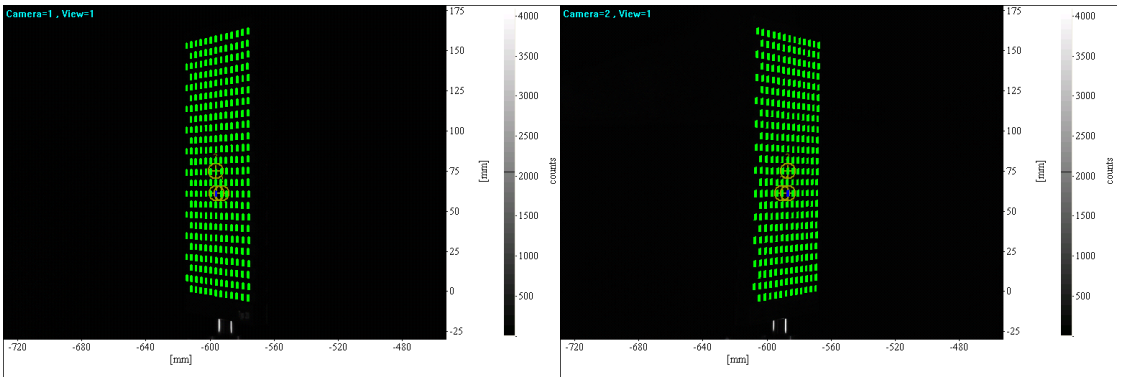

(a) (b)

Figure 2.14 Mark definition and searching for (a) Camera 1 and (b) Camera 2

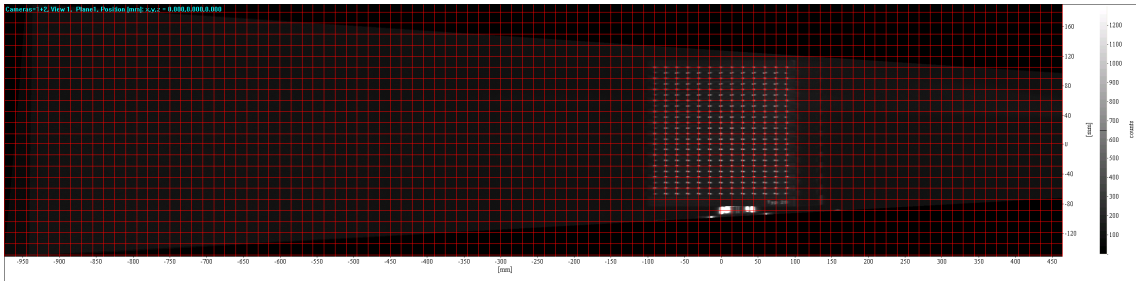

Figure 2.15 Corrected image generated at the end of calibration for the perpendicular plane

2.3.2 Recording

The very first step of recording was to conduct a test run to determine the size of the vector field output image. The camera setting was changed from ‘single frame/single exposure’ to ‘3D cross-correlation’ and the laser was set to trigger from the computer. The air curtain was switched onto its high speed setting, and the door to the test cabin was closed and locked. The seeder was operated for around 15 seconds and all the lights in the lab were turned off. A minute was spent before the test run to allow the seed to distribute uniformly within the cabin.

The interactive mode in DaVis was initiated and a set of images was taken for each camera. The images recorded by the cameras were checked for their intensity range. Normally, intensity values ranging from 100 to 300 counts were deemed ideal for the surveys and the power output from the laser was adjusted till such values are obtained. Next, by alternating between images recorded by either camera, the average motion of the seed between shots was analyzed. Depending on whether the motion of the seed was too little or too much, the time delay between shots was adjusted till satisfactory images are obtained. In the next step, the 'compute vectors' button was clicked and an image containing the velocity vector field was generated in the interactive window. The size of the image was noted down by recalling its properties. With only a small common area being captured by the camera pair, a survey of an entire plane required many such individual common areas to be patched together. The position of the cameras and the lift to record these areas is calculated from the image size previously obtained.

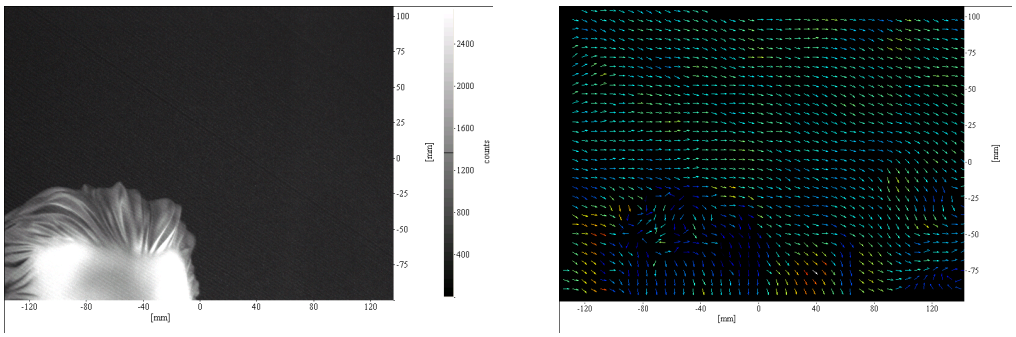

(a) (b)

Figure 2.16 Recordings of a test run with (a) Sample image and (b) Velocity vector field generated thereof

Before beginning recording, the lift was lowered to a height where both the cameras focus on a very small portion of the floor of the test cabin near the plane demarcation. Also, the camera pair was moved such that both focus on a portion of the left edge of the doorway as well. This position was considered, by default, as the first location for recording and the height of the lift platform from the ground and the position of the camera pair on the rails were noted down. The locations of the other positions were calculated relative to this default position.

Based on previous tests, four hundred stereo images were considered adequate at each location in order to obtain ensemble-averaged statistics for the mean and turbulent flow quantities. Starting with the default position, after the ensemble was obtained, the cameras were then moved horizontally to obtain images from the next rectangle and so forth to collect data from the entire row. Upon completing a given row, the lift was raised such that the cameras moved to the next row and the procedure was repeated. Thus all rectangles, positions or common areas pertaining to the entire plane were recorded. The time required for recording at each individual position is around 10 minutes. The total time required to record an entire plane was 10 hours.

Table 2.1 Rows and rectangles per survey plane

Parallel plane	Location of plane from camera plane (mm)	No. of rows and rectangles
1	1846.5	10 X 2
3	1675.0	10 X 4
4	1600.0	10 X 4

The same numbering system as [36] was kept to be consistent. In the present study, surveys were made of planes 1, 3 and 4. Plane 1 was located at the longitudinal axis of the air curtain. Mannequin blockage and limited laboratory access allowed only the right side, i.e. the mannequin's left, to be surveyed. Thus, while recording, the default position was chosen to the right of the center of the doorway and at the floor of the test cabin. Planes 3 and 4 were recorded as explained in the previous paragraph. A single column, consisting of one rectangle per row, located at the center of the air curtain without the manneqin, was surveyed for the perpendicular plane.

2.3.3 Processing

Once the dataset of an entire plane has been recorded, the processing of the same was carried out. First, the calculation of ensemble-averaged velocity vectors was carried out by

batch processing. This process, in-built in DaVis 7.1, required the user to choose the size of interrogation windows for stereo cross-correlation as well as the range of velocities v_x, v_y and v_z for correlation peak validation. The size of the interrogation windows was chosen as 64 pixels by 64 pixels for the parallel planes and 124 pixels by 124 pixels for the perpendicular planes. As the maximum flow velocity, located at the exit of the air curtain, was 5.8 m/s, the range of velocities were set as 0 to 5 m/s for v_x and v_z and 0 to 7 m/s for v_y. Once all the settings for the process have been setup, all datasets in a plane are selected and the processing is engaged. Velocity vector field calculation for a complete plane took around 36 hours. Upon completion, all rectangles were patched together to provide a single, seamless plane, as illustrated in Fig. 2.17. The origin of each plot represents the center of the bottom edge of the air curtain with the green, red and yellow arrows representing the positive x, y and z directions.

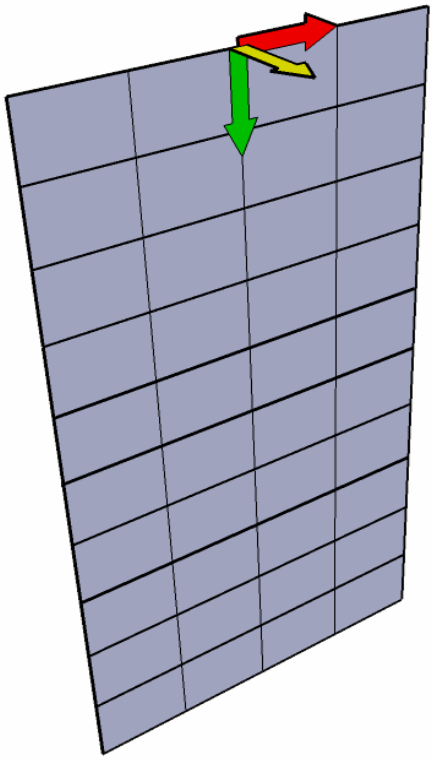

Figure 2.17 Illustration of a plane generated by patching together individual rectangles

Turbulence quantities such as turbulent kinetic energy and Reynolds stresses were calculated from the velocity vector fields at each position using in-built formulas in scalar field processing. The calculation of any turbulence quantity for a complete plane took around one hour. Once again, upon completion, all rectangles were patched together to provide a single, seamless plane.

For the perpendicular plane, only the regions contained by the calibration plate are considered for each of the plots. Adobe Photoshop was employed to carve out these regions and manually stitch them together to get the complete plane. This operation was employed for both the ensemble-averaged velocity vectors and the turbulent kinetic energy plots.

CHAPTER 3

RESULTS

3.1 Discussion of Streamline and Vector Plots

The ensemble-averaged, in-plane streamline maps are shown in Fig. 3.1. The mannequin silhouette or outline is included in the maps as appropriate, while the location of the doorway is shown by the yellow frame. There is a black region at the top of the doorway in the maps, which varies slightly from plane to plane, due to the inability of the system to access a thin region at the exit of the air curtain. Plane 1 shows a distinct shear layer demarcating the air curtain flow from the still ambient environment. Planes 3 and 4 show erratic flow just slightly away from the mannequin. This flow, which is extremely slight as will be shown later, appears to be due to entrainment by the air curtain. Also, the mannequin disturbed the air curtain flow in Plane 1 but the disturbance is not significant in Planes 3 and 4.

The ensemble-averaged, in-plane velocity maps are shown in Fig. 3.2. These velocity maps complement the ensemble-averaged streamline maps of Fig 3.1 and help in understanding how the presence of the mannequin affects the air curtain flow. The velocity map of Plane 1 shows that the jet leaving the air curtain is disrupted by the mannequin. Near the head of the mannequin, the flow stagnates as it approaches the surface. There are regions below the armpit and to the left of the leg where, due to the disruption of the laser, the system was unable to yield good data. The air curtain flow shows a gradual reduction in velocity as it approaches the floor of the test cabin. Also, the data shows large variations in the transverse velocity components at the floor, which can be attributed to the registers covering the floor vents.

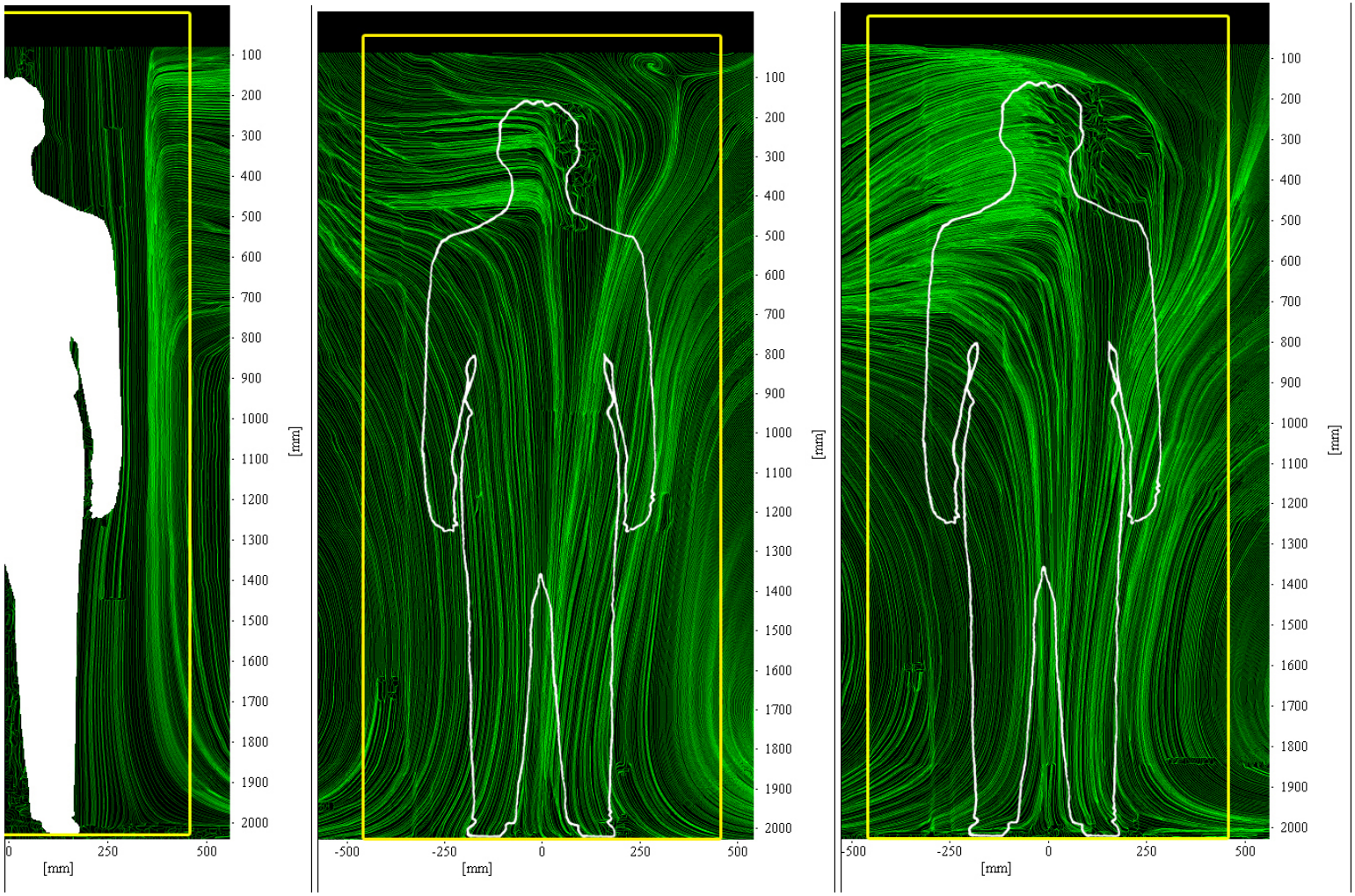

Figure 3.1 Ensemble-averaged streamline plots for (a) Plane 1, (b) Plane 3 and (c) Plane 4

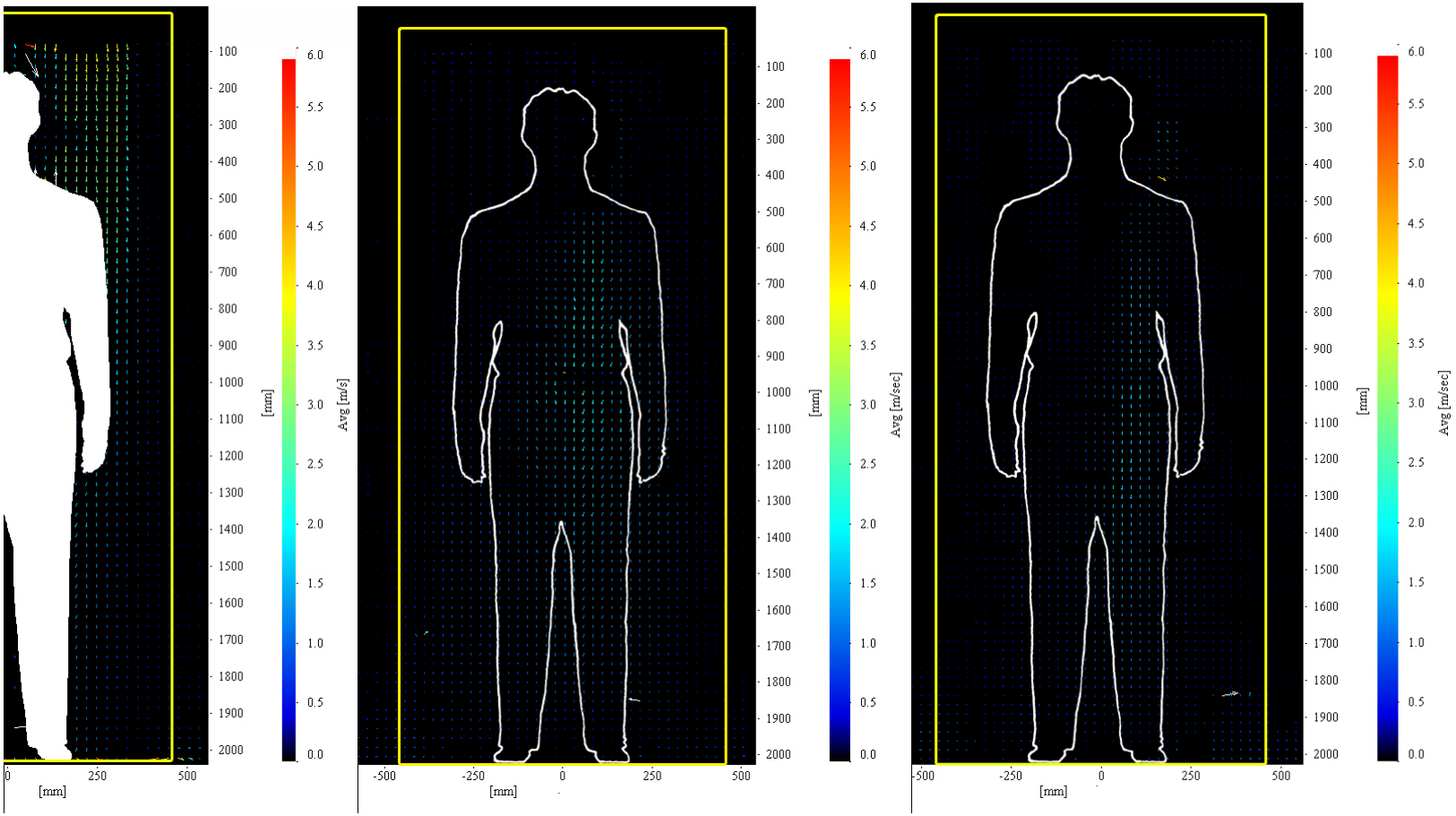

Figure 3.2 Ensemble-averaged velocity vector plots for (a) Plane 1, (b) Plane 3 and (c) Plane 4

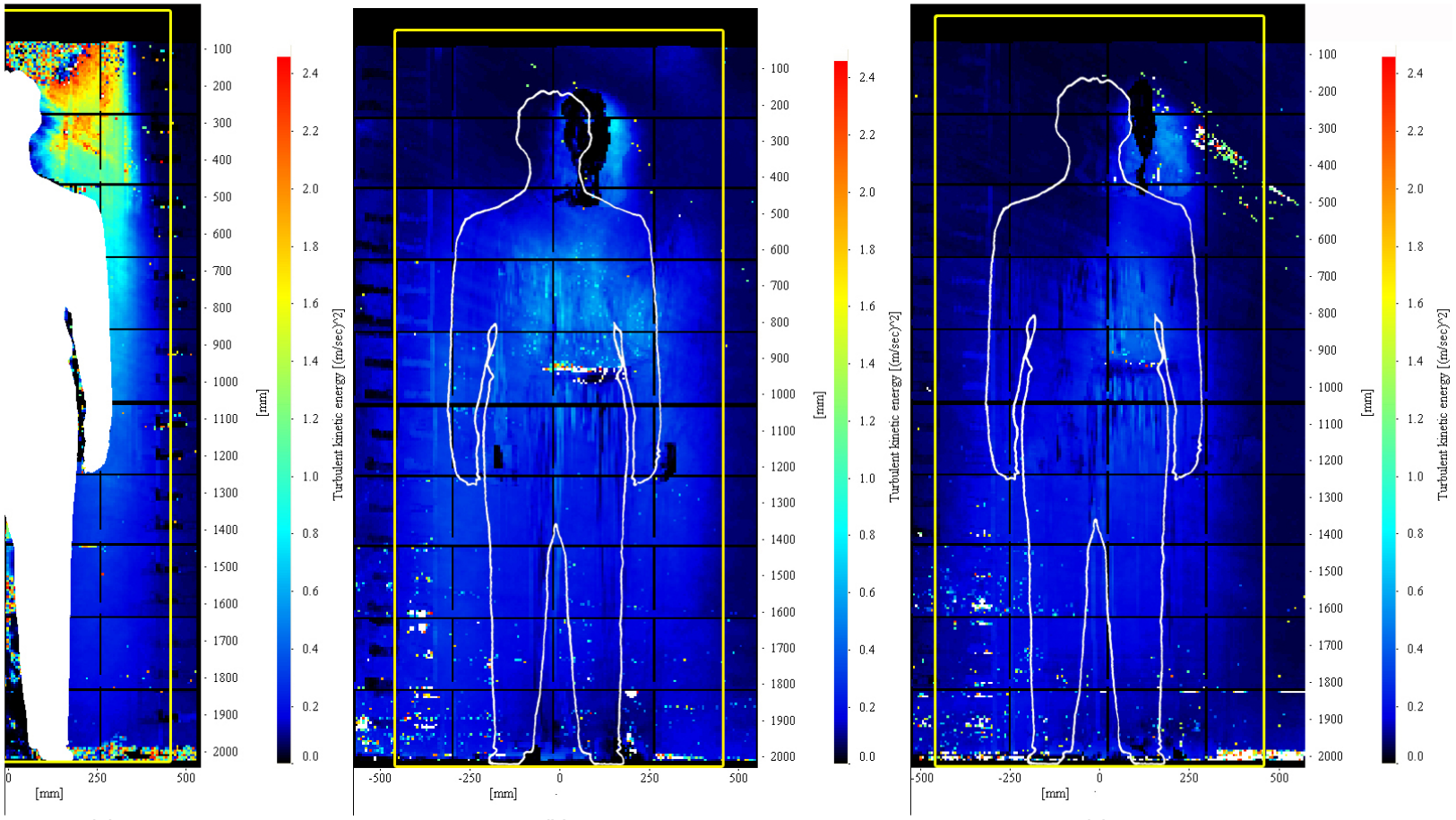

Figure 3.3 Turbulent kinetic energy plots for (a) Plane 1, (b) Plane 3 and (c) Plane 4

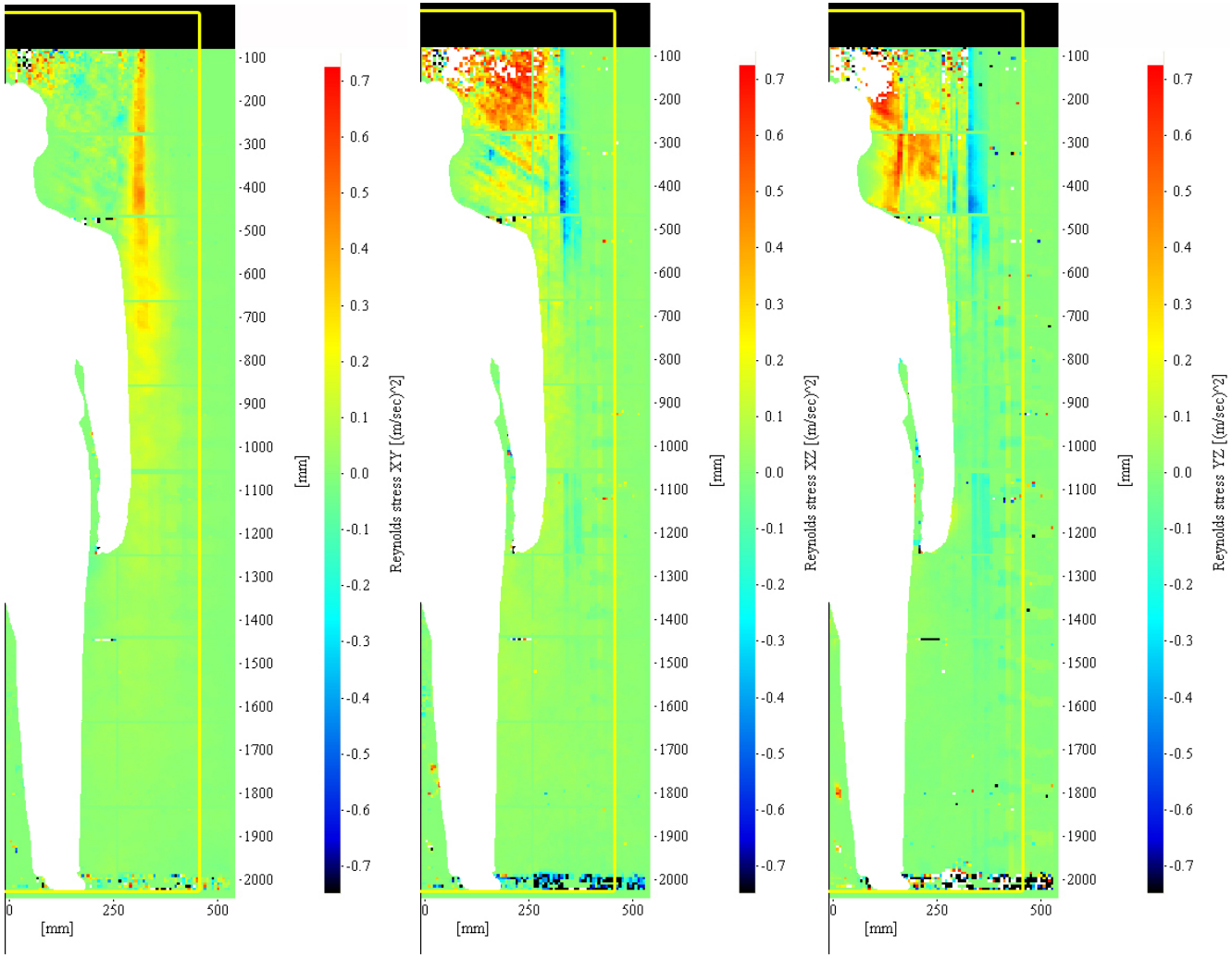

Figure 3.4 Plots of Reynolds stresses (a) XY, (b) XZ and (c) YZ of Plane 1

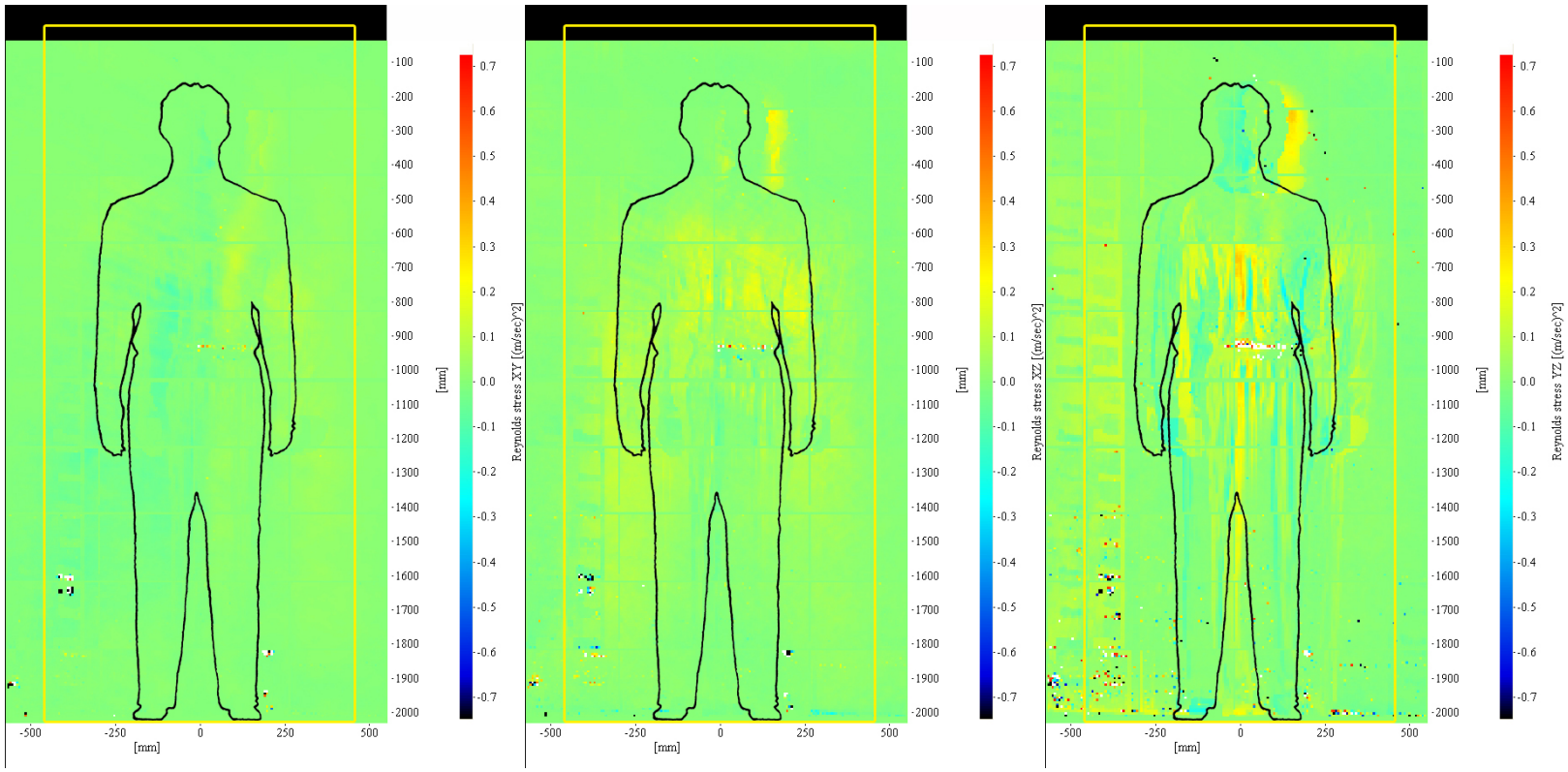

Figure 3.5 Plots of Reynolds stresses (a) XY, (b) XZ and (c) YZ of Plane 3

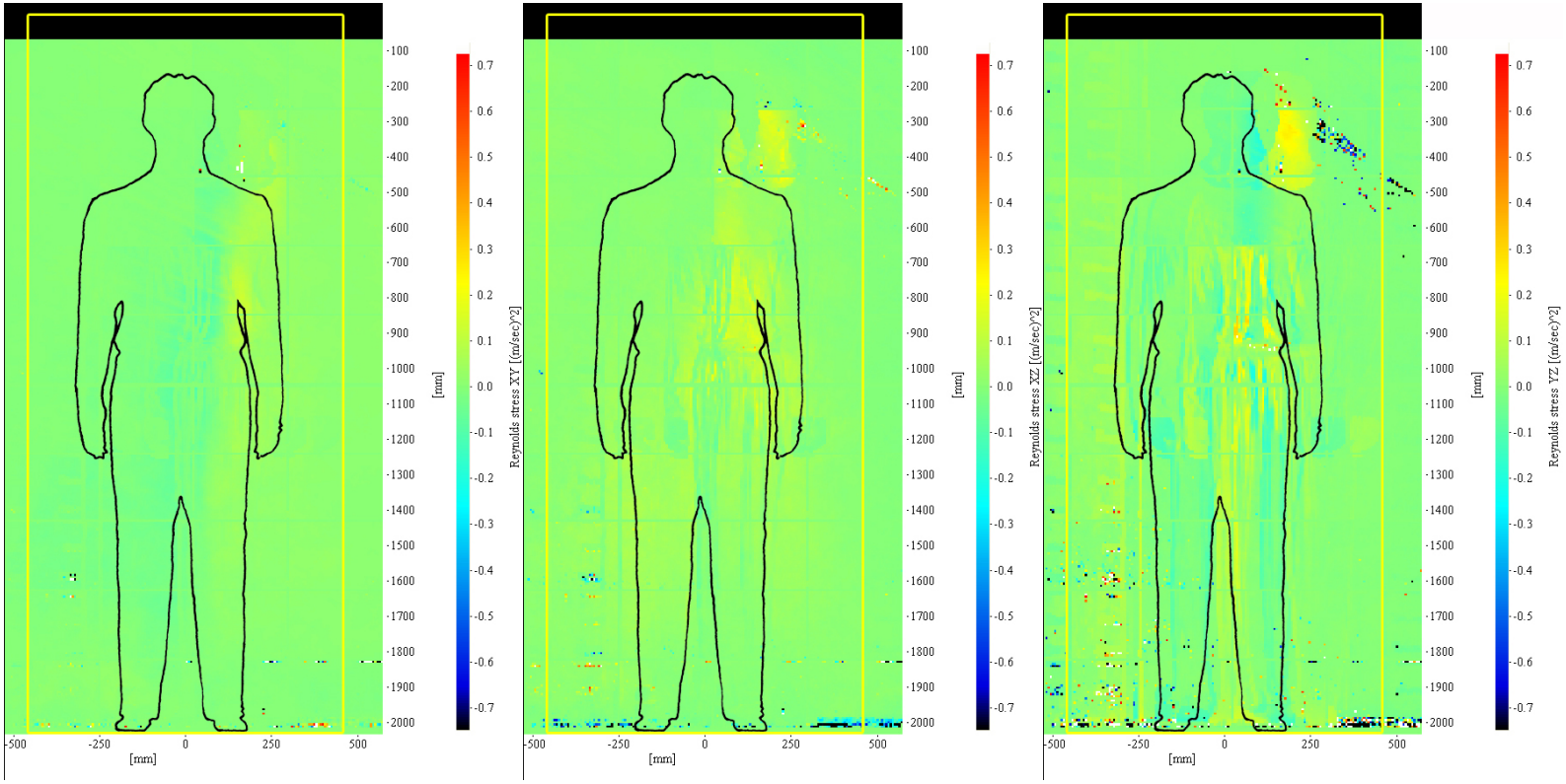

Figure 3.6 Plots of Reynolds stresses (a) XY, (b) XZ and (c) YZ of Plane 4

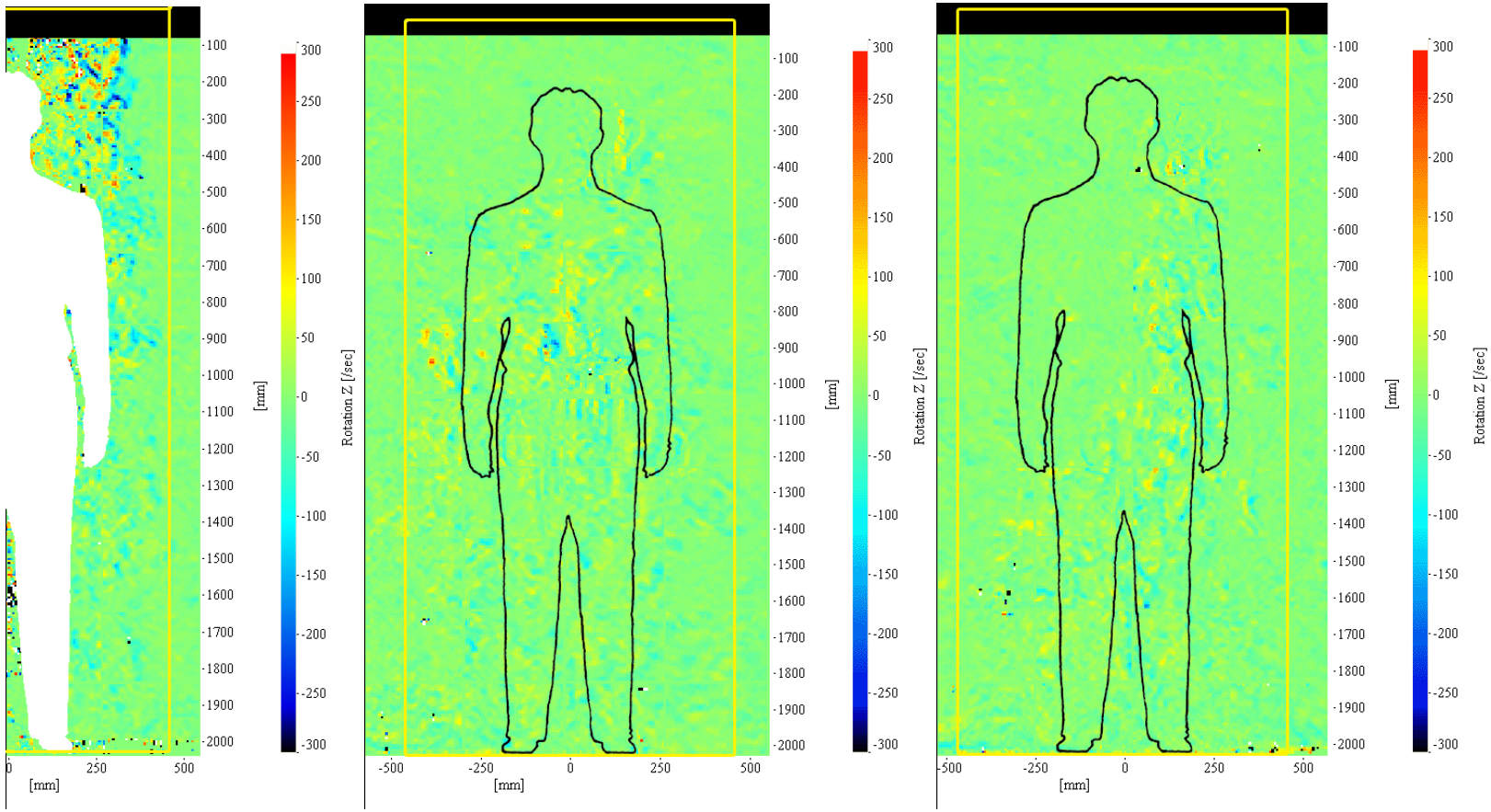

Figure 3.7 Vorticity plots for (a) Plane 1, (b) Plane 3 and (c) Plane 4

The plots for Planes 3 and 4 possess relatively lower velocity magnitudes as compared to Plane 1. This can be attributed to the fact that the air curtain flow diminishes in the z direction towards the cameras. Also, there are regions of relatively higher velocities directly in front of the mannequin and the effects of the registers covering the floor vents are seen to a much lesser extent as compared to Plane 1.

3.2 Discussion of Turbulence Plots

Figure 3.3 shows the turbulent kinetic energy (TKE). For Plane 1, the flow leaving the air curtain is expectedly turbulent. The figures also show that the TKE is generally small and negligible except for regions within the air curtain above the mannequin's shoulder and at the floor vents. Plane 3 shows a triangular artifact to the right of the mannequin which is due to stray scattering from a scratch on the transparent wall. There are dark spots to the right of the mannequin's face and hands. These dark spots are due to laser light reflection from these exposed surfaces even though the laser sheet is shining in planes far from the mannequin. The DaVis software is unable to interrogate those saturated regions and returned no values. Fig 3.3 also shows the patchwork of individual interrogation regions that forms the composite maps which was not evident in the maps of mean properties.

In Fig. 3.4, the Reynolds stress distribution for Plane 1 shows a high region of turbulence as the jet exits the air curtain, as well as at the floor as the flow enters the vents. Fig. 3.4a shows a clear shear layer at the interface of the jet and the surrounding stagnant air. Figs. 3.4b and c also reveal a thin region at the very same position. The Reynolds stress distributions for Planes 3 and 4 are shown in Figs. 3.5 and 3.6. These figures show that there is a negligible amount of turbulence, similar to that shown in the TKE plots.

Figure 3.8 shows the plots of the rotation about z axis component of vorticity. For Plane 1, there is some vorticity around the edges of the upper portion of the mannequin. Similar effects can be seen at the exit of the air curtain as well. However, Planes 3 and 4 contain

negligible vorticity, which ties in with the results of other turbulence quantities for these two planes.

3.3 Perpendicular Plane

The ensemble-averaged, in-plane velocity map is shown in Fig. 3.7a. Its shows a fairly inconsistent velocity distribution towards the top and the stitching of individual rectangles is fairly obvious. There is the presence of circulation at the exit of the air curtain due to interaction with the surrounding stagnant air. The effect of the registers at the floor vents can be seen as well. Fig 3.7b shows the map of turbulent kinetic energy for the perpendicular plane. Turbulence generated at the exit of the air curtain is clearly observed which dissipates gradually as we move towards the floor of the test cabin.

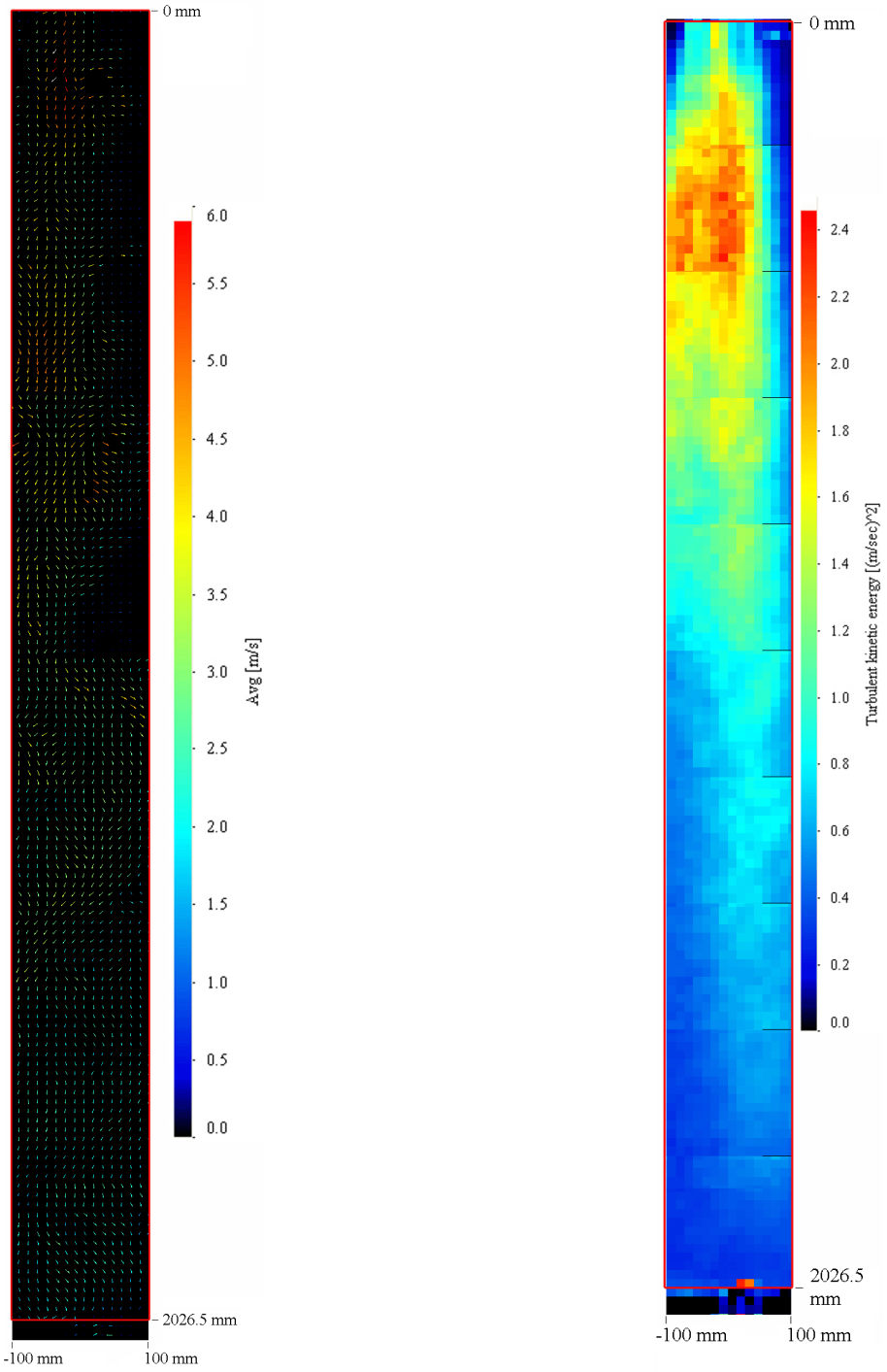

(a) (b)

Figure 3.8 (a) Ensemble-averaged velocity vector and (b) turbulent kinetic energy plots for the perpendicular plane

CHAPTER 4

CONCLUSIONS AND RECOMMENDATIONS

4.1 Conclusions

The flow from a commercial, off-the-shelf air curtain past a mannequin was visualized using stereo particle image velocimetry. A large flow field was successfully mapped and relatively consistent results were obtained. The presence of shiny surfaces caused some regions of the maps to be devoid of useful data.

The study showed that the mannequin, when located directly below the air curtain, disturbed the flow. However, the disturbance was largely confined to the vicinity of the air curtain. The turbulent flow from the air curtain was damped rapidly by the presence of the mannequin. Also, turbulence caused by the presence of the mannequin was present only within and near the exit of the air curtain.

4.2 Recommendations and Future Work

The effects of reflections off exposed surfaces of the mannequin can be reduced by spray-painting these regions flat black. Reflections are also caused by folds in the mannequin's apparel which can be countered by either using clothes that are 100% cotton or removing them and painting the entire surface. By making the cabin portable or providing space on either side, both sides of Plane 1 may be surveyed. For the perpendicular plane, a test run should be conducted to determine the size of the dataset required to obtain consistent plots like those of the parallel planes.

Future work may include numerically modeling the flow.

REFERENCES

1. Lawton E, Howell R. Energy savings using air curtains installed in high traffic doorways. *ASHRAE Transactions,* Vol. 101, No. 2, pp. 136-143, 1995.
2. Cui J, Wang S. Application of CFD in evaluation and energy-efficient design of air curtains for horizontal refrigerated display cases. *International Journal of Thermal Sciences.* Vol. 43, No. 10, pp. 993-1002, 2004.
3. Costa JJ, Oliveira LA, Silva MCG. Energy savings by aerodynamic sealing with a downward-blowing plane air curtain – A numerical approach. *Energy and Buildings*, Vol. 38, No. 10, pp. 1182-1193, 2006.
4. Foster AM, Swain MJ, Barrett R, James SJ. Experimental verification of analytical and CFD predictions of infiltration through cold store entrances. *International Journal of Refrigeration,* Vol. 26, No. 8, pp. 918-925, 2003.
5. Foster AM, Swain MJ, Barrett R, D'Agaro P, James SJ. Effectiveness and optimum jet velocity for a plane jet air curtain used to restrict cold room infiltration. *International Journal of Refrigeration,* Vol. 29, No. 5, pp. 692-299, 2006.
6. Chen Y, Yuan X. Experimental study of the performance of single-band air curtains for a multi-deck refrigerated display cabinet. *Journal of Food Engineering,* Vol. 69, No. 3, pp. 261-267, 2005.
7. D'Agaro P, Cortella G, Croce G. Two- and three-dimensional CFD applied to vertical display cabinets simulation. *International Journal of Refrigeration,* Vol. 29, No. 2, pp. 178-190, 2006.
8. Zhihov A, Skistad H, Mundt E, Posokhin V, Ratcliff M, Shilkrot E, Strongin A. Principles of air and contaminant movement inside and around buildings. In: Industrial Ventilation Design Handbook, H.D. Goodfellow, E. Tähti (eds.), Academic, San Diego, 2001.
9. Carlson DA, Hogsette JA, Kline DL, Geden CD, Vandermeer RK. Prevention of mosquitoes (diptera: culicidae) and house flies (dipteral: muscidae) from entering simulated aircraft with commercial air curtain units. *Journal of Economic Entomology,* Vol. 99, No. 1, pp. 182-193, 2006.
10. Robertson P, Shaw BH. Linear air curtain as a particulate barrier. *Journal of Environmental Science,* Vol. 21, No. 3, pp. 32-33, 1978.
11. Rojeski J. Improving indoor air quality by increased ventilation effectiveness. *Journal of Architectural Engineering,* Vol. 5, No. 1, pp. 25-29, 1999.
12. Rydock JP, Hestad T, Haugen H, Skaret JE. An isothermal air curtain for isolation of smoking areas in restaurants. In: Air Distribution in Rooms, ROOMVENT 2000, Proceedings of 7th International Conference on Ventilation for Health and Sustainable Environment, Awbi HB (ed.) Elsevier, Amsterdam, 2000.
13. Pavageau M, Nieto EM, Rey C. Odour and VOC confining in large enclosures using air curtain devices. *Water Science and Technology,* Vol. 44, No. 9, pp. 165-171, 2001.
14. Hestroni G, Hall CW, Dhanak AM. Heat transfer properties of an air curtain. *Transactions of the American Society of Agricultural Engineers,* Vol. 6, pp. 328-334, 1963.
15. Hayes FC, Stoecker WF. Design data for air curtains. *ASHRAE Transactions,* Vol. 75, No. 2, pp. 168-180, 1969.

16. Etkin B, Goering PLE. Air-curtain walls and roofs – 'dynamic' structures. *Philosophical Transactions of the Royal Society of London, Series A, Mathematical and Physical Sciences,* Vol. 269, No. 1199, pp. 527-543, 1971.
17. Field BS, Loth E. Entrainment of refrigerated air curtains down a wall. *Experimental Thermal and Fluid Science,* Vol. 30, No. 3, pp. 175-184, 2006.
18. Navaz HK, Amin N, Rasipuram SC, Faramarzi R. Jet entrainment minimization in an air curtain of open refrigerated display case. *International Journal of Numerical Methods for Heat and Fluid Flow,* Vol. 16, No. 4, pp. 417-430, 2006.
19. Hu SC, Wu YY, Liu CJ. Measurements of air flow characteristics in a full-scale clean room. *Building and Environment,* Vol. 31, No. 2, pp. 119-128, 1996.
20. Kotrappa P, Bhanti DP. Smoke puff generator for room air movement studies. *American Industrial Hygiene Association Journal,* Vol. 28, No. 2, pp. 171-174, 1968.
21. Field BS, Loth E. An air curtain along a wall with high inlet turbulence. *Journal of Fluids Engineering,* Vol. 126, No. 3, pp. 391-398, 2004.
22. Navaz HK, Faramarzi R, Gharib M, Dabiri D, Modarress D. The application of advanced methods in analyzing the performance of the air curtain in a refrigerated display case. *Journal of Fluids Engineering,* Vol. 124, No. 3, pp. 756-764, 2002.
23. Rouaud O, Havet M, Solliec C. Influence of external perturbations on a minienvironment: Experimental investigations. *Building and Environment,* Vol. 39, No. 7, pp. 863-872, 2004.
24. Neto LPC, Silva MCG, Costa JJ. On the use of infrared thermography in studies with air curtain devices. *Energy and Buildings,* Vol. 38, No. 10, pp. 1194-1199, 2006.
25. Pavageau M, Loubiére K, Gupta S. Automatic education and statistical analysis of coherent structures in the wall region of a confined plane turbulent impinging jet. *Experiments in Fluids,* Vol. 41, No. 1, pp. 35-55, 2006.
26. Bhattacharjee P, Loth E. Simulations of laminar and transitional cold wall jets. *International Journal of Heat and Fluid Flow,* Vol. 25, No. 1, pp. 32-43, 2004.
27. Foster AM, Madge M, Evans JA. The use of CFD to improve the performance of a chilled multi-deck retail display cabinet. *International Journal of Refrigeration,* Vol. 28, No. 5, pp. 698-705, 2005.
28. Welling I, Andersson I-M, Rosen G, Räisänen J, Mielto T, Marttinen K, Niemelä R. Contaminant dispersion in the vicinity of a worker in a uniform velocity field. *Annals of Occupational Hygiene,* Vol. 44, No. 3, pp. 219-225, 2000.
29. Flynn MR, Sills ED. Numerical simulation of human exposure to aerosols generated during compressed air spray-painting in cross-flow ventilated booths. *Journal of Fluids Engineering,* Vol. 123, No. 1, pp. 64-70, 2001.
30. Nielsen PV. Computational fluid dynamics and room air movement. *Indoor Air,* Vol. 14, No. 7, pp. 134-143, 2004.
31. Xing H, Hatton A, Awbi HB. A study of the air quality in the breathing zone in a room with displacement ventilation. *Building and Environment,* Vol. 36, No. 7, pp. 809-820, 2001.
32. Lundgren L, Skare L, Lidén C, Tornling G. Large organic aerosols in a dynamic and continuous whole-body exposure chamber tested on humans and on a heated mannequin. *Annals of Occupational Hygiene,* Vol. 50, No. 7, pp. 705-715, 2007.
33. Lee E, Khan JA, Fiegley CE, Ahmed MR, Hussey JR. An investigation of air inlet types in mixing ventilation. *Building and Environment,* Vol. 42, No. 3, pp. 1089-1098, 2007.
34. Wang A, Zhang Y, Sun Y, Wang X. Experimental study of ventilation effectiveness and air velocity distribution in an aircraft cabin mockup. *Building and Environment,* Vol. 43, No. 3, pp. 337-343, 2008.
35. Craven BA, Settles GS. A computational and experimental investigation of the human plume. *Journal of Fluids Engineering,* Vol. 128, No. 6, pp. 1251-1258, 2006.

36. Lu FK, Pierce AJ. Visualizing the flow induced by an air curtain using stereo particle image velocimetry. *Proc ISFV13 - 13th International Symposium of Fluid Visualization,* Paper 234, July 1-4, 2008.
37. Adrian RJ. Twenty years of particle image velocimetry. *Experiments in Fluids,* Vol. 39, No. 2, pp. 159-169, 2005.
38. Raffel M, Willert C, Wereley S, Kompenhans J. In: Particle Image Velocimetry: A Practical Guide, 2nd Edition, pp. 128, Verlag Berlin Heidelberg, Springer, 1998.
39. Keane RD, Adrian RJ. Cross-correlation analysis of particle image fields for velocity measurements. *American Society of Mechanical Engineers, Fluids Engineering Division (Publication) FED,* Vol. 128, *Experimental and Numerical Flow Visualization,* pp. 1-8, 1991.

BIOGRAPHICAL INFORMATION

John Edward Fernandes was born on June 4, 1984 in Mumbai, India, the youngest of two sons. He attended St. Dominic Savio High School, Mumbai till the 10^{th} grade and passed securing a first class with distinction and 83.33%. Having chosen Science as his stream of study, John spent the next two years at Chauhan Institute of Science, Mumbai before graduating from the 12^{th} grade. Possessing a keen interest in automobiles and design, in August 2002 he chose to pursue a bachelor's degree in Mechanical Engineering at Fr. Conceicao Rodrigues Institute of Technology, Vashi, Navi Mumbai. In August 2006, John graduated with a Bachelor of Engineering in Mechanical Engineering. Wanting to study further, in Fall 2006 he enrolled into UTA to obtain his Master of Science in Mechanical Engineering. John plans on obtaining a few years of industrial experience before returning to his country. His main areas of professional interest include fluid dynamics, flow visualization and computational fluid dynamics.